

Effect of Cooling Rate on δ -Ferrite Formation and Sigma Precipitation Behavior of 254SMO Super-Austenitic Stainless Steel During Solidification



YUNONG LI, DENING ZOU, MIAOMIAO LI, LIBO TONG, YINGBO ZHANG,
and WEI ZHANG

The formation of δ -ferrite and the precipitation behavior of the sigma phase during the solidification of 254SMO super-austenitic stainless steel (SASS) were investigated at five typical cooling rates (6 °C/min to 1000 °C/min) *via* high-temperature confocal scanning laser microscopy (HT-CSLM). The results showed that the 254SMO steel featured a significant dendritic solidified structure. With increasing cooling rates from 6 °C/min to 1000 °C/min, the initial solidification temperature and the secondary dendrite arm spacing (SDAS) of 254SMO gradually decreased and could be expressed as a function of cooling rates, the average sizes of SDAS were 113.33, 57.05, 34.98, 32.84 and 14.04 μm . δ -ferrite was formed through a divorced eutectic reaction in the late solidification stage and existed in the interdendritic region. As the cooling rate increased, the δ -ferrite phase content in the steel sample first decreased from 3.610 (6 °C/min) to 0.051 pct (100 °C/min) and then increased slightly to 0.089 pct (1000 °C/min). The sigma phase was formed from the solid-state phase transition of δ -ferrite. With increasing cooling rates, the variation trend of the sigma phase content was opposite to that of the δ -ferrite phase. The solidification mechanism of 254SMO at the five typical cooling rates was explored. Moreover, the distributions of Cr, Ni, and Mo in the solidified 254SMO SASS were characterized *via* electron probe microscopy. Cr and Mo were segregated in the interdendritic region, while Ni was clustered in the dendritic region.

<https://doi.org/10.1007/s11663-023-02927-w>

© The Minerals, Metals & Materials Society and ASM International 2023

I. INTRODUCTION

OWING to their excellent mechanical properties and resistance to pitting and intergranular corrosion, super-austenitic stainless steels (SASSs) have widespread applications.^[1–4] For example, they are used in the offshore industry, desalination processes, seawater treatment, the manufacture of chlorine-containing bleaching equipment, and flue gas desulfurization. However, the high-alloy composition of SASS leads to a complex metallurgical phase transformation process and intricate solid phase transformation process and solidification microstructure formation.^[5] The higher content of Mo

element in SASS increases the precipitation tendency of δ -ferrite and sigma brittle phases during solidification,^[6–9] which significantly influences the hot working properties and corrosion resistance of the steel.^[10] However, the formation and precipitation behavior of the second phase formed during the solidification process of SASS is rarely reported. Studies have shown that changing the cooling rate is a vital method for controlling the content of the second phase.^[11–13] Therefore, investigating the influence of cooling rates on the precipitation behavior of δ -ferrite and sigma phases formed in the solidified SASS to improve product quality is vital.

Studies have mainly focused on the effect of cooling rate on the formation of ferrite phases during the solidification process of ordinary austenitic stainless steel. Fu *et al.*^[5] studied the influence of different cooling rates on the microstructural evolution of solidified 304 steel and confirmed that dendritic ferrite can be formed at the bottom of the sample under lower cooling rates. Li *et al.*^[14] confirmed that with increasing cooling rate, the volume fraction of δ -ferrite increased. Presently, the research on the solidification process of SASS is still at a relatively basic stage. However, the formation of

YUNONG LI, DENING ZOU, MIAOMIAO LI, and LIBO TONG are with the School of Metallurgical Engineering, Xi'an University of Architecture and Technology, Xi'an, 710055 Shaanxi, P.R. China. Contact e-mail: zoudening@sina.com YINGBO ZHANG is with the Jilin Railway Technology College, Jilin 132200, P.R. China. WEI ZHANG is with the Shanxi Taigang Stainless Steel Co., Ltd., Taiyuan, 030003 Shanxi, P.R. China.

Manuscript submitted June 6, 2023; accepted September 18, 2023.
Article published online October 2, 2023.

Table I. Composition of 254SMO Steel (Weight Percent)

C	Si	Mn	P	S	Cr	Ni	Mo	N	Cu	Fe
0.02	0.26	0.25	0.02	0.26	20.15	17.73	6.12	0.21	0.71	bal.

δ -ferrite and sigma phases in SASS during solidification remains unclear, and the relationship between their morphology, distribution, and content with cooling rate is undefined. Therefore, this study provides significant guidance for controlling the solidification process of SASS and producing high-quality materials.

In this study, the continuous-casting billet of 254SMO that produced from Taigang Stainless Steel Factory was taken as the research object. Firstly, combined with the cooling rate range of slow solidification ($0.1\text{ }^{\circ}\text{C/s}$) and sub-rapid solidification technology ($10^2\text{ }^{\circ}\text{C/s}$) in the current mature stainless steel preparation technology, the cooling rate in this paper was $6\text{ }^{\circ}\text{C/min}$ to $1000\text{ }^{\circ}\text{C/min}$, the solidification process and microstructural evolution of 254SMO SASS were observed *via* HT-CSLM. Secondly, the microstructure after solidification was observed *via* optical microscopy (OM) and SDAS was measured *via* ImagePro-Plus to establish the functional relationship between cooling rate, initial solidification temperature, and SDAS. Meanwhile, the precipitation behavior of δ -ferrite and sigma phase was characterized *via* scanning electron microscopy (SEM), energy-dispersive spectroscopy (EDS) and electron backscattering diffraction (EBSD), and compared with the actual casting billet used in this paper. Finally, the distribution of Cr, Mo and Ni in solidified 254SMO were analyzed *via* electron probe microanalysis (EPMA), in order to clarify the effect of cooling rate on the solidification structure and the formation, distribution and content of precipitated phase in 254SMO. Therefore, this study provides significant guidance for improving the quality of 254SMO SASS and clarifying their complex solidification mechanism under five cooling rates.

II. EXPERIMENTAL PROCEDURES

A. Material Preparation

The test steel continuous-casting billet was purchased from Shanxi Taigang Stainless Steel Co., Ltd. Table I shows the composition of the 254SMO steel.

B. HT-CSLM Experiments

HT-CSLM (VL2000DX-SVF18SP) was used to investigate the microstructural evolution of 254SMO at five typical cooling rates. Samples with the sizes of $\Phi 7.8 \times H 3.0$ mm cylinder were used. Before the HT-CSLM experiment was conducted, the samples were subjected to grinding, polishing, cleaning, and drying processes. The treated samples were loaded into an alumina crucible and placed in the HT-CSLM instrument chamber under a high-purity argon atmosphere (99.999 pct, the flowrate was 300 ml/min). Before the experiment,

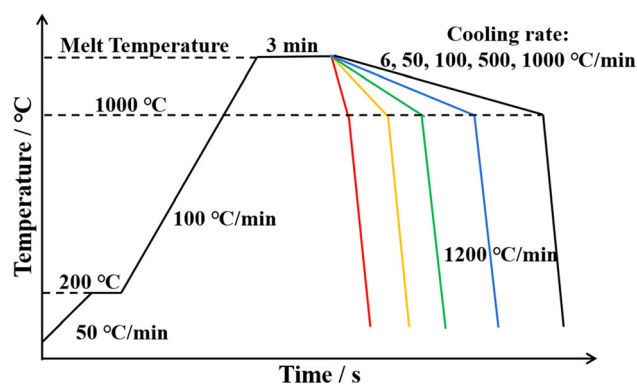


Fig. 1—Experimental process of HT-CSLM.

the vacuum pump was used to pump vacuum for three times and the pure iron with fixed melting point was used for temperature calibration. Subsequently, the sample was heated at $50\text{ }^{\circ}\text{C/min}$ from room temperature to $200\text{ }^{\circ}\text{C}$, and then the heat was increased to a melting temperature at $100\text{ }^{\circ}\text{C/min}$. The sample was held for 3 minutes to ensure complete melting. Afterward, the sample was cooled to $1000\text{ }^{\circ}\text{C}$ (the solid phase ratio was 1 that the sample was completely solidified) under five cooling rates ($6\text{ }^{\circ}\text{C/min}$, $50\text{ }^{\circ}\text{C/min}$, $100\text{ }^{\circ}\text{C/min}$, $500\text{ }^{\circ}\text{C/min}$, and $1000\text{ }^{\circ}\text{C/min}$) and finally cooled to room temperature at $1200\text{ }^{\circ}\text{C/min}$. Figure 1 presents the experimental process. The sample temperature was controlled using a B-type thermocouple placed below the crucible. The real-time information on the sample phase transformation was stored during the entire process, and one photo was collected per second. The microstructures of samples subjected to HT-CSLM experiments were analyzed.

C. Microstructure Characterization

The samples prepared for OM were subjected to five typical cooling rates and then ground, polished, and etched with 10 pct oxalic acid for 60 seconds (at a 6 V, 500 mA). Subsequently, the samples were rinsed with alcohol and dried. The dendritic morphology of the samples was observed using an Olympus-PM3 microscope, and the SDAS was calculated using the Image-Pro Plus. The morphology and distribution of precipitated phases in the sample were observed *via* backscattering diffraction (BSD). The phase composition of samples used for HT-CSLM was analyzed *via* EDS and EBSD coupled with field emission scanning electron microscopy (Zeiss Gemini SEM 300). For EBSD analysis, the samples were subjected to electropolishing with a 9:1 mixture of alcohol and perchloric acid at 30 V, 400 to 500 mA for 1 min. The element distribution in the samples was analyzed *via* EPMA (EPMA-1720 h, Shimadzu, Japan).

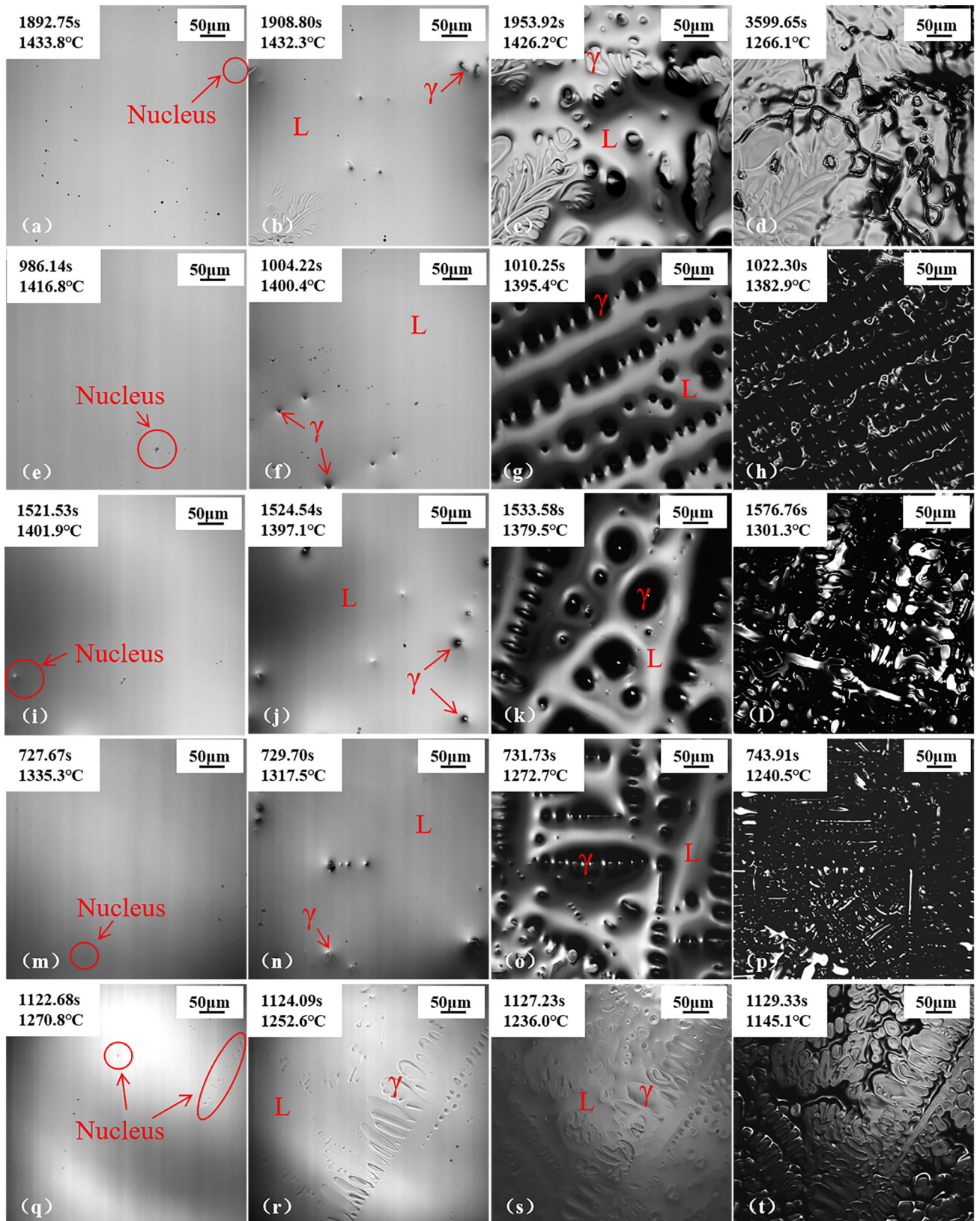


Fig. 2—Solidification process of 254SMO via HT-CSLM: (a) through (d) 6 °C/min; (e) through (h) 50 °C/min; (i) through (l) 100 °C/min; (m) through (p) 500 °C/min; (q) through (t) 1000 °C/min.

III. RESULTS AND DISCUSSION

A. Influence of Cooling Rate on Supercooling

Figure 2 shows the microstructural evolution during the solidification process of 254SMO under different cooling rates. As the temperature decreased to the initial solidification temperature rates, the austenite phase first nucleated from the liquid phase. Moreover, as the temperature decreased, the austenite nuclei increased, and the grains grew gradually,^[15] eventually forming austenite dendrites. As solidification progressed, the solid-liquid interface gradually moved toward the

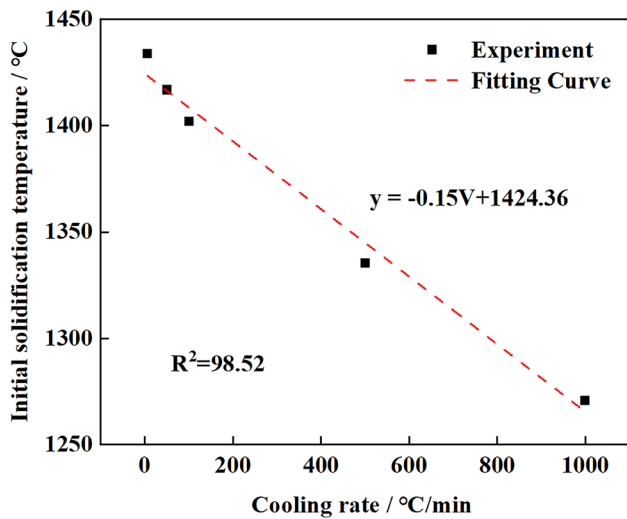


Fig. 3—Initial solidification temperature under different cooling rates.

interdendritic regions. When the liquid phase completely disappeared, the interdendritic region transformed into a solid state. The interdendritic regions were the main areas of δ -ferrite and sigma phase formation in the late solidification stage.

The initial solidification temperature of 254SMO gradually decreased as the cooling rate increased, indicating that it was a function of the cooling rate.^[16] Perepezko *et al.*^[17] and Wielgosz *et al.*^[18] found that the actual crystallization temperatures of materials were consistently lower than the theoretical temperatures, resulting in the supercooling phenomenon. With increasing cooling rates, the undercooling and nucleation rates increased, leading to the lowering of the initial solidification temperature.^[19] This affected the diffusion of elements in the sample during solidification and the grain size after solidification. Figure 3 showed the functional relationship between the initial solidification temperature and cooling rate in this work. Through the fitting and analysis of the experimental data, the function was obtained as $y = -0.15V + 1424.36$. The cooling rate affected the initial solidification temperature, while supercooling influenced the evolution of the solidified microstructure of the sample. Therefore, the cooling rate significantly affected the formation of the δ -ferrite and sigma phases during the late solidification stage.

B. Influence of Cooling Rate on the Microstructures

The OM image of 254SMO (Figure 4) at different cooling rates showed that the 254SMO steel featured dendritic microstructures after the HT-CSLM experiment. Moreover, as the cooling rate increased, the

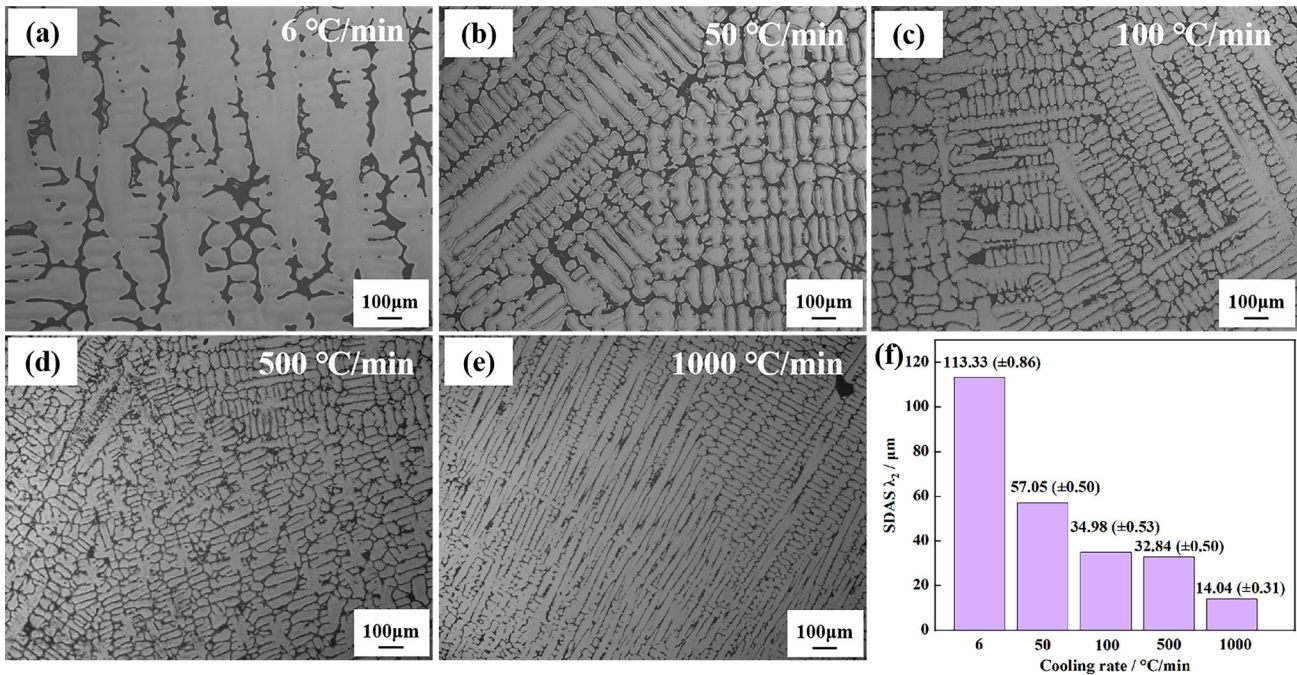


Fig. 4—OM image of sample microstructures: (a) 6 °C/min; (b) 50 °C/min; (c) 100 °C/min; (d) 500 °C/min; (e) 1000 °C/min; (f) SDASs at different cooling rates.

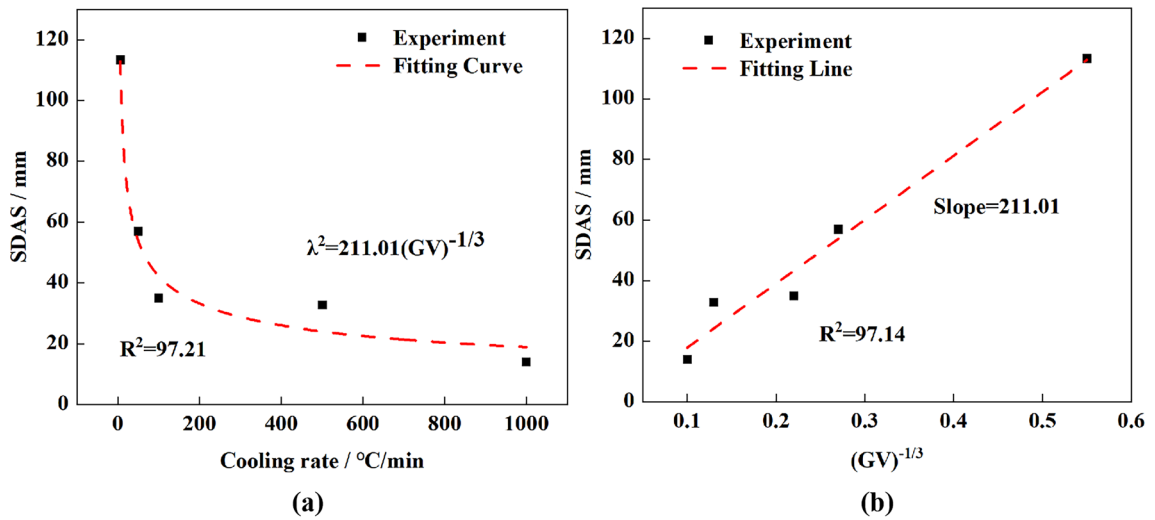


Fig. 5—SDAS values at different cooling rates: (a) relationship between SDAS and cooling rate; (b) relationship between SDAS and $(GV)^{-1/3}$.

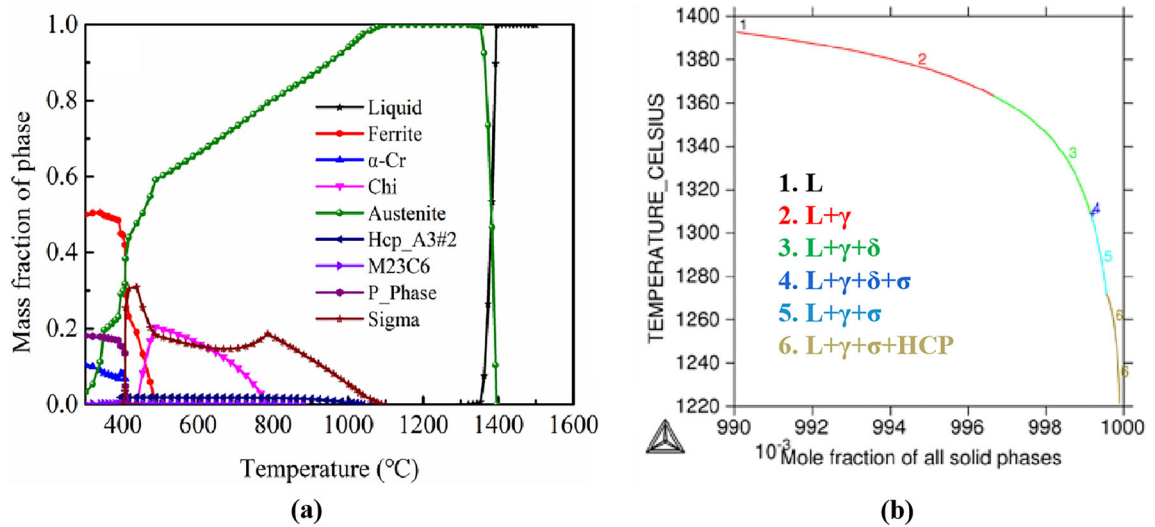


Fig. 6—Phase diagram of thermodynamic equilibrium: (a) thermal equilibrium phase diagram; (b) solidification path of Scheil-Gulliver module.

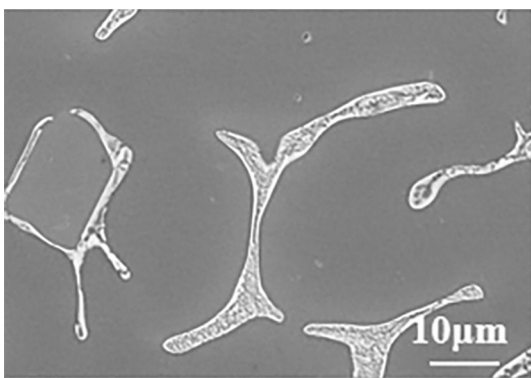


Fig. 7—Ferrite morphology obtained via scanning electron microscopy.

dendritic structure of the steel became finer, and SDAS decreased (Figure 4(f)). The relationship between the SDAS and cooling rate of austenitic stainless steel can be expressed as $\lambda_2 = K \times v^{-n}$.^[17] According to Figure 5, the relationship between SDAS and cooling rate is expressed as $\lambda_2 = 211.01(GV)^{-1/3}$, where λ_2 is SDAS, μm , and GV is the cooling rate, $^\circ\text{C}/\text{min}$ (Figure 5).

The thermal equilibrium phase diagram of 254SMO calculated using FactSage is shown in Figure 6(a). The matrix structure of 254SMO mainly comprised austenite and other precipitated phases such as sigma, α -Cr, Pi-phase, and $M_{23}C_6$. As the solidification process progressed, austenite began to precipitate at 1392.57 $^\circ\text{C}$. As the temperature cooled to 1322.44 $^\circ\text{C}$, the amount of austenite in the steel rapidly increased, and

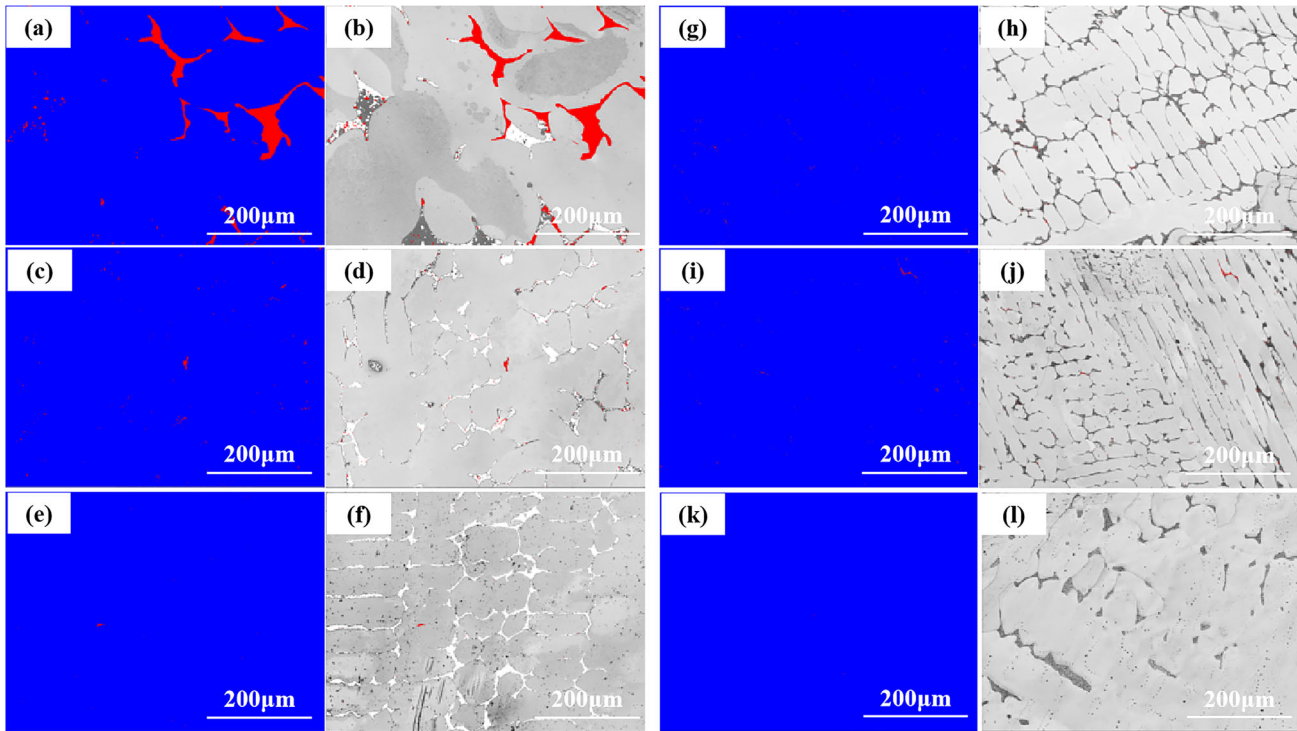


Fig. 8—EBSD characterization of ferrite phase: (a) and (b) 6 °C/min; (c) and (d) 50 °C/min; (e) and (f) 100 °C/min; (g) and (h) 500 °C/min; (i) and (j) 1000 °C/min; (k) and (l) actual cast 254SMO billet.

Table II. δ -Ferritic Phase Content

Cooling Rates (°C/min)	Content of δ -Ferritic Phase (Pct)
6	3.610
50	0.210
100	0.051
500	0.073
1000	0.089
Actual Billet	0.002

all the liquid phases gradually transformed into austenite; thus, the single-phase austenite existed in the high-temperature region. As the temperature decreased to 1088.4 °C, the sigma phase first precipitated from the austenite phase. The content of the sigma phase gradually increased as the temperature decreased, reaching the maximum of 31.16 pct at 442 °C. The sigma phase was present in a temperature range of 1088 °C to 405 °C. As the temperature decreased, the α -Cr, Pi-phase, and $M_{23}C_6$ phases began to precipitate, but their content was relatively small, making them less relevant to the main focus of this study. Ferrite was precipitated at 482.5 °C and gradually increased with decreasing temperature.

The thermal equilibrium phase diagram showed that 254SMO underwent A-type solidification. The solidification path of 254SMO simulated using Scheil–Gulliver module of Thermo-Calc was $L \rightarrow L + \gamma \rightarrow L + \gamma + \delta \rightarrow L + \gamma + \delta + \sigma \rightarrow L + \gamma + \sigma \rightarrow L + \gamma + \sigma + Hcp$ (Figure 6(b)). The Scheil–Gulliver solidification path indicates that 254SMO underwent AF-type solidification. Figure 6 shows that the solidification modes of 254SMO under equilibrium and non-equilibrium conditions were different. This can be attributed to the effect of high alloying on Mo segregation during the solidification of 254SMO. Moreover, the large atomic radius of Mo hindered its diffusion during solidification. The Scheil model assumes that during solidification, complete diffusion occurs in the liquid phase and no diffusion occurs in the solid phase. Therefore, 254SMO undergoes AF-type solidification under actual conditions.

The austenitic stainless steel featured high-alloy content and complex elemental compositions. According to the contents of Cr_{eq} and Ni_{eq} , the steel can be simplified to Fe–Cr–Ni ternary systems. The solidification modes of stainless steel can be classified into the following four types based on Cr_{eq}/Ni_{eq} values.^[20]

F mode : $L \rightarrow L + \delta \rightarrow \delta \rightarrow \delta + \gamma (Cr_{eq}/Ni_{eq}) > 1.95$

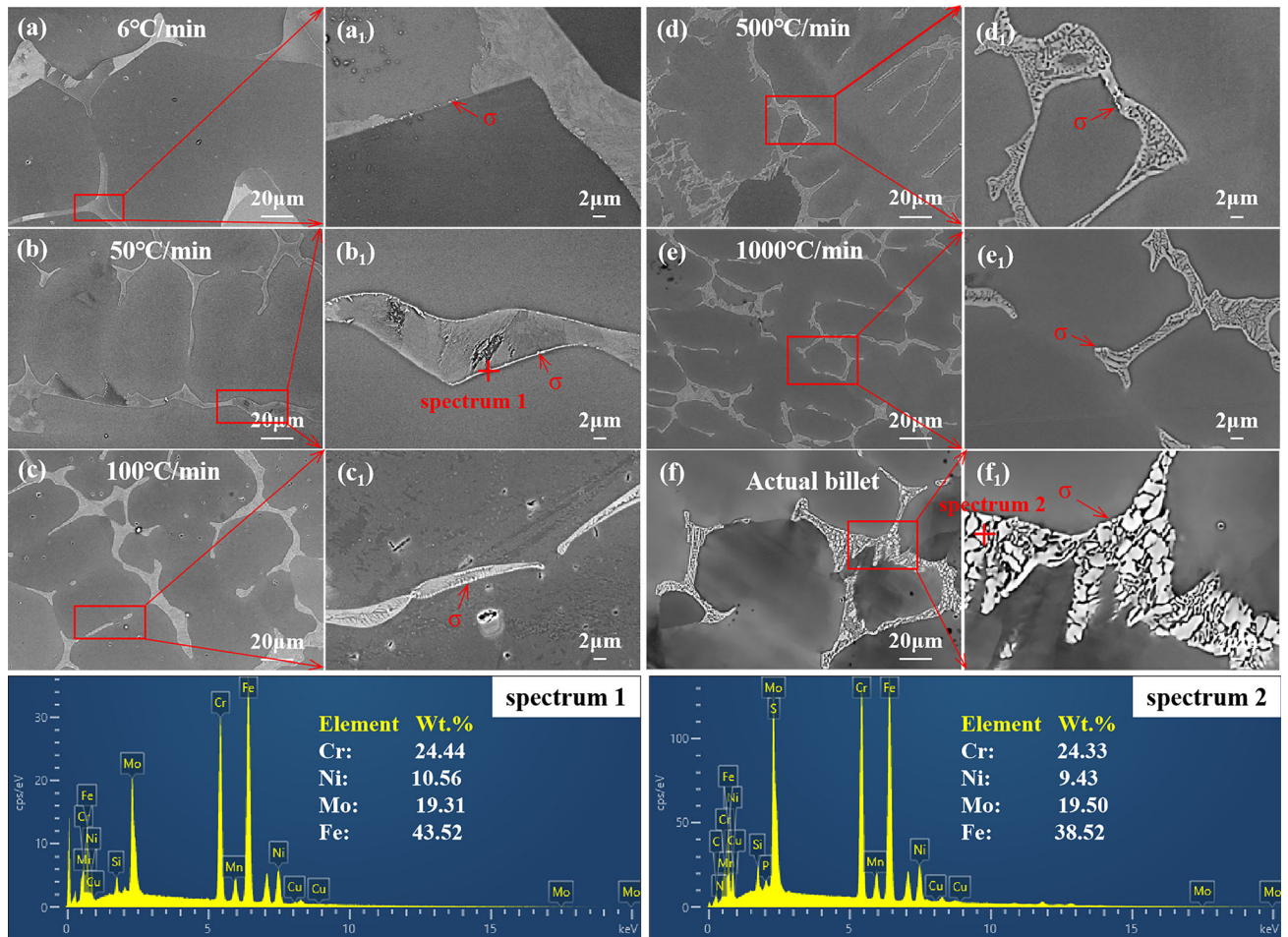
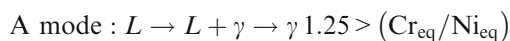
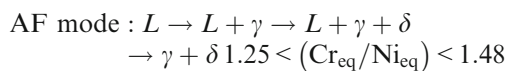
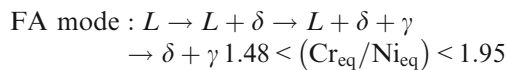


Fig. 9—Microstructure morphology of sigma phase: (a) and (a₁) 6 °C/min; (b) and (b₁) 50 °C/min; (c) and (c₁) 100 °C/min; (d) and (d₁) 500 °C/min; (e) and (e₁) 1000 °C/min; (f) and (f₁) actual cast 254SMO billet.



where the L liquid phase, δ -ferrite, γ -austenite, Cr_{eq} , and Ni_{eq} are calculated according to the following formula:

According to the above formula, the 254SMO continuous-casting billets used in this study featured Cr_{eq} , Ni_{eq} , and $\text{Cr}_{\text{eq}}/\text{Ni}_{\text{eq}}$ values of 26.660, 18.395, and 1.450, respectively. The solidification mode of the 254SMO steel was AF-type, indicating that the austenite phase was first precipitated from the liquid phase, consistent with the precipitation sequence in the Scheil–Gulliver module.

According to its actual solidification mode, the microstructure of 254SMO mainly comprised austenitic, δ -ferrite, and sigma phases. During the HT-CSLM analysis, no δ -ferrite precipitation was observed in the sample microstructure (Figure 2). However, the solidification path simulated using the Scheil module showed that high-temperature δ -ferrite precipitated in the late solidification stage. δ -ferrite was independently distributed among the interdendritic regions and did not interweave with austenitic structures, showing typical divorced eutectic precipitate features (Figure 7). This indicates that δ -ferrite was obtained from the divorced eutectic reaction during the late solidification stage.

The EBSD characterization of the δ -ferrite phase is presented in Figure 8. Figures 8(a) through (j) show the sample with controlled cooling rates obtained *via* HT-CSLM. Figures 8(k) through (l) show the sample obtained from the actual cast billet of 254SMO used in this study. In the figures, blue represents the austenite phase, and red denotes the δ -ferrite phase. Moreover, the actual cast billet contained a minimal amount of δ -ferrite (Table II). However, with increasing cooling rates, the δ -ferrite phase in the samples with controlled cooling rates *via* HT-CSLM first decreased and then

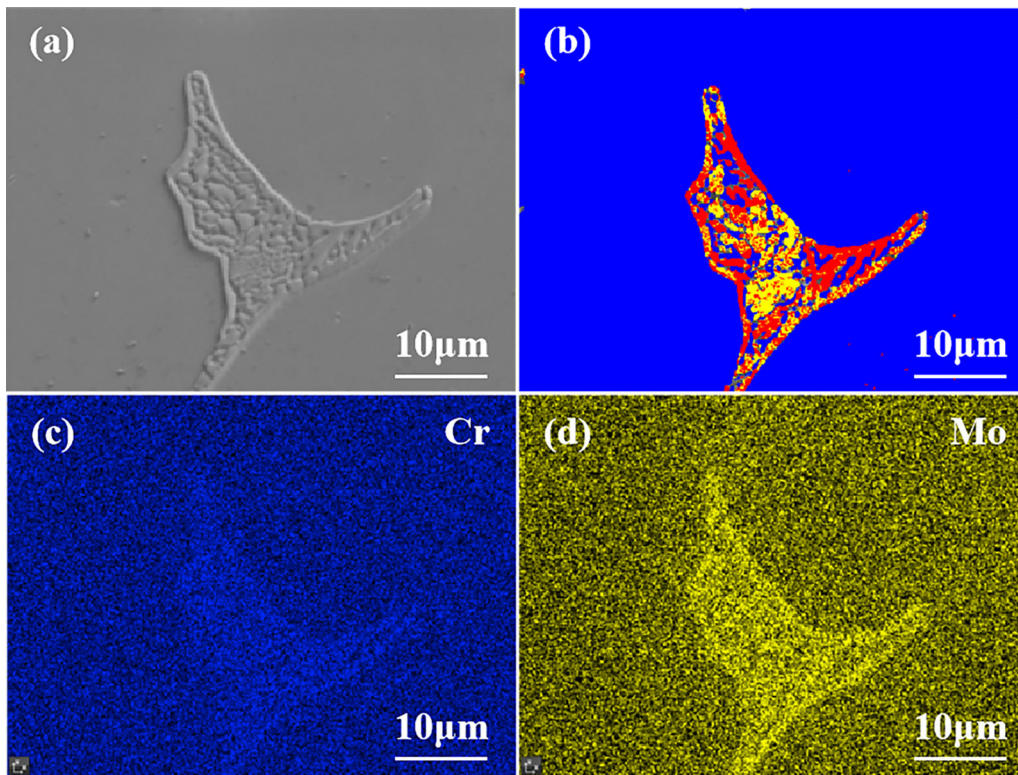


Fig. 10—EBSD maps of phase identification: (a) Original drawing of EBSD; (b) phase identification; (c) map scanning photo of Cr; (d) map scanning photo of Mo.

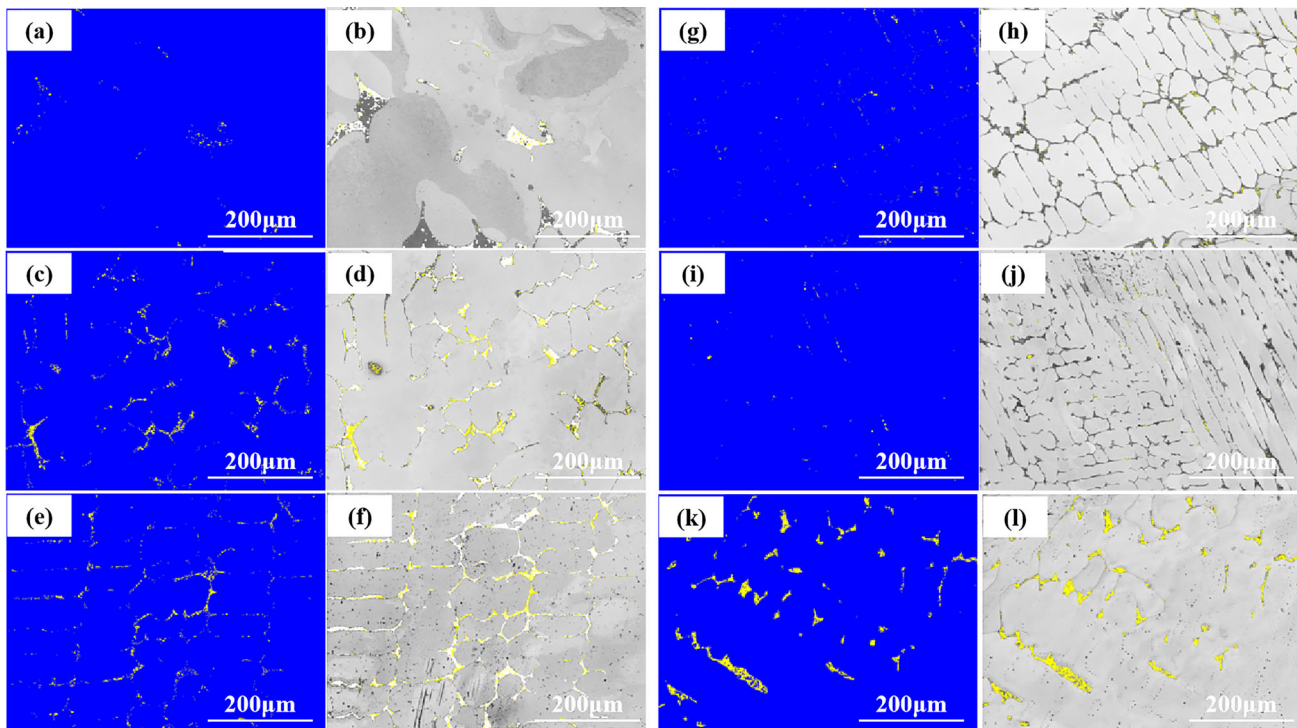


Fig. 11—EBSD microstructures of sigma phase: (a) and (b) 6 °C/min; (c) and (d) 50 °C/min; (e) and (f) 100 °C/min; (g) and (h) 500 °C/min; (i) and (j) 1000 °C/min; (k) and (l) actual cast billet of 254SMO.

Table III. Sigma Phase Content

Cooling Rates (°C/min)	Content of Sigma Phase (Pct)
6	0.136
50	0.949
100	1.363
500	0.384
1000	0.129
Actual Billet	2.475

increased, primarily existing in the interdendritic region. This can be attributed to the restricted atomic diffusion ability at higher cooling rates, leading to the accumulation of numerous Cr and Mo elements (formation elements of δ -ferrite) in the interdendritic region after solidification. Thus, the precipitation of the δ -ferrite phase mainly occurred in the interdendritic region. The formation of δ -ferrite is closely related to SDAS.^[14] As SDAS decreased with increasing cooling rate, it promoted the dissolution of δ -ferrite phases and reduced their content. However, at higher cooling rates, the divorced eutectic reaction process was accelerated during the late solidification period. Consequently, the δ -ferrite phase had no time to dissolve and the solidification process ended. Therefore, the δ -ferritic phase was retained and its content was slightly increased.

The sigma phase in Fe–Cr–Mo mainly comprised elements with the content range of Fe 30.8 to 33.0 wt pct, Cr 22.8 to 29.8 wt pct, and Mo 13.5 to 28.4 wt pct.^[21] The BSD of the sigma phase (Figure 9), combined with EDS point quantitative analysis, revealed that the element composition of the sigma phase in the sample at different cooling rates after HT-CSLM was the same as that in the actual cast billet. However, the morphologies of the sigma phase in the samples and the actual cast billet were different. The bright white region in the samples subjected to HT-CSLM corresponded to the sigma phase. The sigma phase in the solidified 254SMO featured a small size and was distributed between interdendritic and dendritic regions growing around the δ -ferritic phase (Figures 9(a) and (e₁)). This indicates that the sigma phase was formed through the solid-phase transformation after solidification. However, the sigma phase in the actual cast billet (Figures 9(f) and (f₁)) exhibited a flaky structure with a large size and was continuously distributed at the grain boundary. In a previous study, the second phase directly precipitated during solidification displayed a larger size.^[22] Thus, it is speculated that the sigma phase in the actual cast billet was directly precipitated during the solidification process.

Figure 10 shows the EBSD analysis of eutectic products at different cooling rates after HT-CSLM. In the figure, blue represents the austenitic phase, red denote the ferritic phase, and yellow represents the sigma phase. Both ferritic and sigma phases were present and interleaved in the eutectic products (Figure 10(b)). Additionally, the eutectic products mainly contained Cr and Mo-rich phases (Figures 10(c) and

(d)), consistent with the elemental characteristics of ferrite and sigma phases. The position and size of the sigma phase (Figures 9(a) through (e₁)) combined with the EBSD analysis, (Figure 10) revealed that $\delta \rightarrow \sigma + \gamma_2$ was formed from the solidified ferrite phase.

Figure 11 displays the microstructures of the sigma phase examined *via* EBSD. Figures 11(a) through (j) show the sample with a controlled cooling rate *via* HT-CSLM. Figures 11(k) and (l) show the sample obtained from the actual cast billet of 254SMO. In the figure, blue represents the austenite phase, and yellow denotes the sigma phase. Moreover, the actual cast billet featured a higher sigma phase content, about 2.475 pct, while the samples displayed relatively small sigma phase contents at different cooling rates after HT-CSLM (Table III). As the cooling rates increased, the sigma phase content in the samples first increased and then decreased. This was attributable to the decrease in the initial solidification temperature with increasing cooling rates, which leads to the limited atomic diffusion capacity during the solidification process.^[23] Hence, numerous Cr and Mo elements accumulated in the residual liquid phase. Moreover, SDAS decreased with increasing cooling rates, accelerating the dissolution of δ -ferrite and promoting the nucleation of sigma phases. However, as the cooling rate further increased, the δ -ferrite phase had no time to dissolve, hindering the nucleation and growth of the sigma phase^[24]; consequently, the sigma phase content first increased and then decreased. As the cooling rates increased, the contents of δ -ferrite and sigma phases exhibited an opposite trend, confirming the conversion of δ -ferrite into the sigma phase (Tables II and III).

The solidification process of 254SMO is shown in Figure 12. As the solidification process progressed, the austenite phases first nucleated from the liquid phase, forming austenitic dendrites. Moreover, Cr and Mo were repelled to the liquid phase and the solid–liquid interface,^[25] where the peak of δ -ferrite phase nucleation is reached. The δ -ferrite phase was obtained through the divorced eutectic reaction at the late solidification stage and was distributed in the interdendritic region. Subsequently, the liquid phase disappeared, and the solidification process ended. As the temperature decreased, the δ -ferrite gradually transformed into the sigma phase. The actual solidification process can be summarized as follows:

The austenitic phase precipitated from the liquid phase was represented as $L \rightarrow L + \gamma_1$.

The austenite attached to the primary dendritic structure gradually grew and increased. At the late solidification stage, the separate eutectic reaction occurred, leading to the precipitation of the δ -ferrite phase, $L \rightarrow L + \gamma_1 \rightarrow L + \gamma_1 + \delta$.

As the temperature decreased, the solidification process ended, and the liquid phase disappeared, $L \rightarrow L + \gamma_1 \rightarrow L + \gamma_1 + \delta \rightarrow \gamma_1 + \delta$.

As the temperature further decreased, the δ -ferrite phase transformed into sigma and austenite phases, $L \rightarrow L + \gamma_1 \rightarrow L + \gamma_1 + \delta \rightarrow \gamma_1 + \delta \rightarrow \gamma_1 + \delta + \sigma + \gamma_2$.

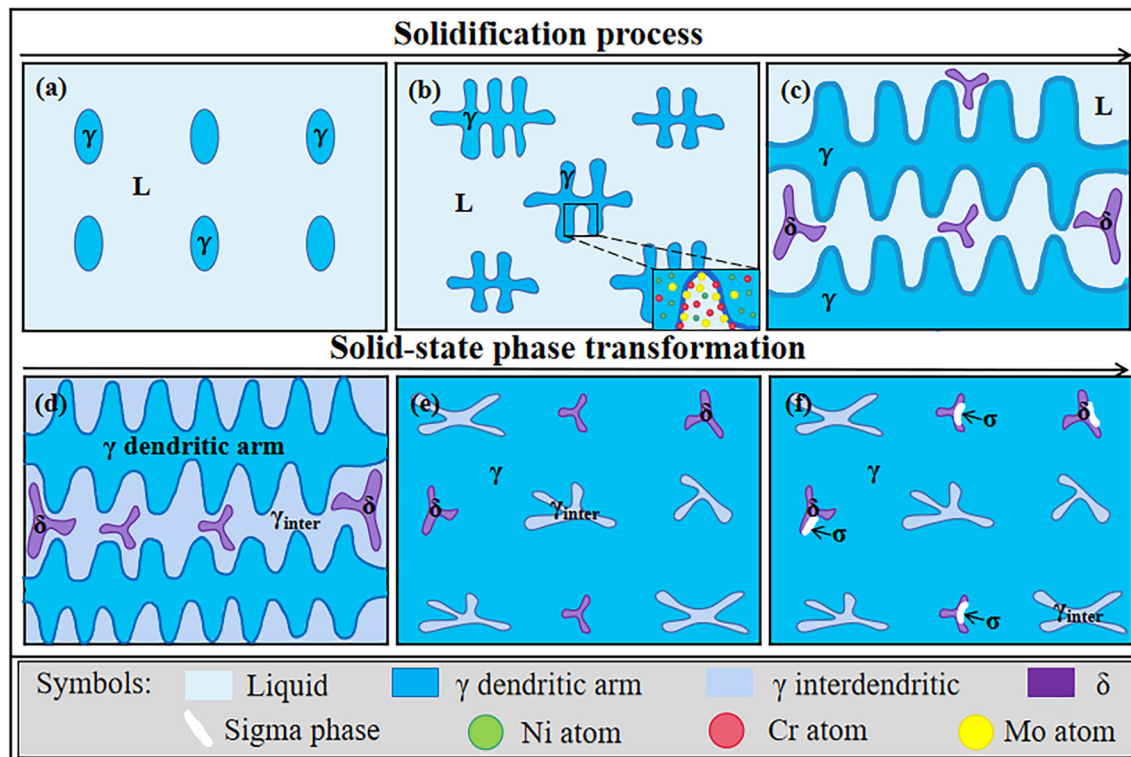


Fig. 12—Diagram of solidification process of 254SMO: (a) austenite nucleation; (b) formation of austenite dendrites; (c) divorced eutectic reaction generating δ -ferrite; (d) disappearance of the liquid phase at the end of solidification; (e) ferrite phase decomposition; (f) formation of sigma phase.

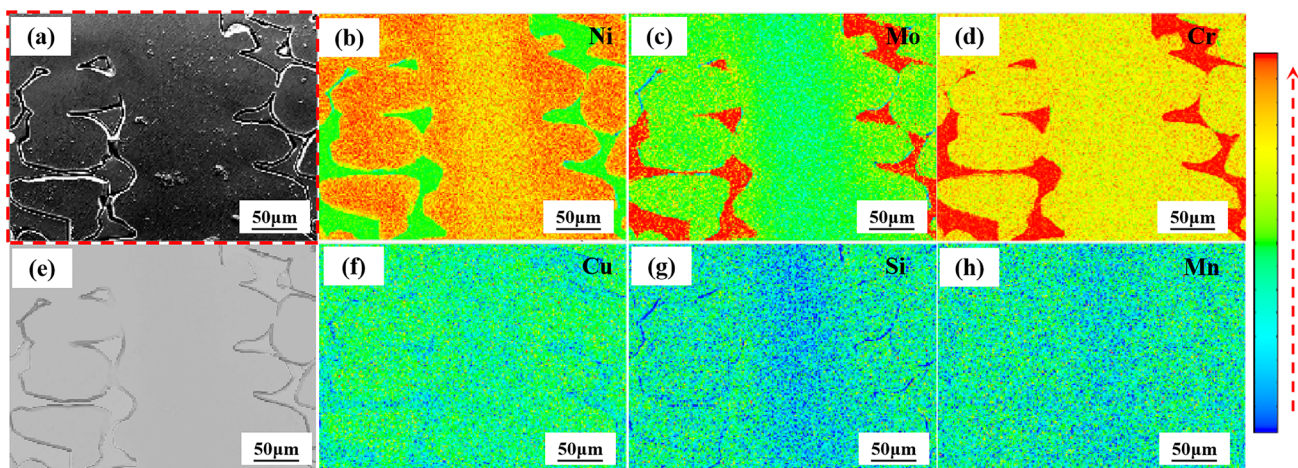


Fig. 13—EPMA map scanning photos of elements at 6 °C/min: (a) surface scanning of dendritic area; (b) Ni; (c) Mo; (d) Cr; (e) original diagram of dendrite; (f) Cu; (g) Si; (h) Mn.

C. Element Distribution

During the solidification progress, the inhomogeneous redistribution of alloying elements into the solid and liquid phases leads to microsegregation.^[26] The EPMA surface scanning images of HT-CSLM samples with a cooling rate of 6 °C/min is presented in Figure 13. The Cr, Mo, and Si elements were mainly concentrated in the interdendritic region, while Ni and Cu were

concentrated in the dendritic region. Among various elements, Mn was evenly distributed with minimal segregation. However, significant segregation phenomena occurred in the Cr, Ni, and Mo elements. Moreover, Cr and Mo elements mainly formed the sigma and δ -ferrite phases. The segregation position of Cr and Mo was consistent with the formation position of the sigma and δ -ferrite phases.

IV. CONCLUSIONS

The solidified microstructure of 254SMO SASS under different cooling rates was investigated *via* HT-CSLM. The solidified structures of the steel were characterized *via* OM, scanning electron microscopy, EBSD, and EPMA, and microstructural evolution was analyzed through a combination of the characterization results and thermodynamic software. This study elucidated the solidification process of 254SMO steel and investigated the precipitation behavior of sigma and δ -ferrite phases. The main conclusions are as follows:

1. The 254SMO steel featured a significant solidified dendritic structure, and through HT-CSLM experiments, the functional relationships of the initial solidification temperature and SDAS with the cooling rate were established as $y = -0.15V + 1424.36$ and $\lambda_2 = 211.01(\text{GV})^{-1/3}$.
2. The δ -ferrite phase was formed through the divorced eutectic reaction at the late solidification stage of 254SMO. As the cooling rate increased, the δ -ferrite phase content first decreased and then increased.
3. The sigma phase was formed from the δ -ferrite phase transition. As the cooling rate increased, the sigma phase content first decreased and then increased.
4. The distribution of elements in the solidified 254SMO was examined *via* EPMA analysis. The results revealed that Cr, Mo, and Si were mainly concentrated in the interdendritic region, while Ni and Cu were concentrated in the dendritic region. However, Mn was evenly distributed with minimal segregation.

ACKNOWLEDGMENTS

The authors acknowledge support of this work by the National Natural Science Foundation of China (51774226), the Major Program of Science and Technology in Shanxi Province (Nos. 20191102006 and 202202050201019), the Shaanxi Outstanding Youth Fund project (Grant Number 2021JC-45) and Key international cooperation projects in Shaanxi Province (Grant Number 2020KWZ-007).

CONFLICT OF INTEREST

The authors declare no conflict of interest.

REFERENCES

1. K.H. Lo, C.H. Shek, and J.K.L. Lai: *Mater. Sci. Eng. R Rep.*, 2009, vol. 65, pp. 39–104.
2. Y.S. Hao, W.C. Liu, and Z.Y. Liu: *Acta Metall. Sin. Eng.*, 2018, vol. 31, pp. 401–14.

3. Y. Hao, W. Liu, and J. Li: *Mater. Sci. Eng. A*, 2018, vol. 736, pp. 258–68.
4. M.J. Perricone and J.N. Dupont: *Metall. Mater. Trans. A*, 2006, vol. 37, pp. 1267–80.
5. J.W. Fu, Y.S. Yang, J.J. Guo, and W.H. Tong: *Mater. Sci. Technol.*, 2008, vol. 24, pp. 941–44.
6. M. Torkar, F. Vodopivec, and S. Petovar: *Mater. Sci. Eng. A*, 1993, vol. 173, pp. 313–16.
7. P.L. Dong, H.X. Shang, and H. Wang: *China Metall.*, 2017, vol. 27, pp. 7–13.
8. R.W. Fonda, E.M. Lauridsen, W. Ludwig, P. Tafforeau, and G. Spanos: *Metall. Mater. Trans. A*, 2007, vol. 38, pp. 2721–26.
9. C. Lee, S. Roh, C. Lee, and S. Hong: *Mater. Chem. Phys.*, 2018, vol. 207, pp. 91–97.
10. A. Lescur, E. Stergar, J. Lim, S. Hertel'e, and R.H. Petrov: *Mater. Charact.*, 2021, vol. 182, p. 111524.
11. M. Bleckmann, J. Gleinig, J. Hufenbach, H. Wendrock, L. Giebeler, J. Zeisig, U. Diekmann, J. Eckert, and U. Kühn: *J. Alloys Compd.*, 2015, vol. 634, pp. 200–07.
12. D.S. Petrović, G. Klannik, M. Pirnat, and J. Medved: *J. Therm. Anal. Calorim.*, 2011, vol. 105, pp. 251–57.
13. D.S. Petrović, M. Pirnat, G. Klančnik, P. Mrvar, and J. Medved: *J. Therm. Anal. Calorim.*, 2012, vol. 109, pp. 1185–91.
14. X. Li, F. Gao, J.H. Jiao, G.M. Cao, Y. Wang, and Z.Y. Liu: *Mater. Charact.*, 2021, vol. 174, p. 111029.
15. W.L. Wang, T.F. Luo, Z.H. Liu, and M.Y. Zhu: *Metall. Mater. Trans. B*, 2023, vol. 54B, pp. 776–92.
16. Y.S. Hao, J. Li, X. Li, W.C. Liu, G.M. Cao, C.G. Li, and Z.Y. Liu: *J. Mater. Process. Technol.*, 2020, vol. 275, pp. 116326–35.
17. J.H. Perepezko and G. Wilde: *Curr. Opin. Solid St. M.*, 2016, vol. 20, pp. 3–12.
18. E. Wielgosz and T. Kargu: *J. Therm. Anal. Calorim.*, 2015, vol. 119, pp. 1547–53.
19. T. Liu, M.J. Long, D.F. Chen, Y.W. Huang, J. Yang, H.M. Duan, L.T. Gui, and P. Xu: *Metall. Mater. Trans. B*, 2020, vol. 51B, pp. 338–52.
20. A.D. Schino, M.G. Mecozzi, and M. Barteri: *J. Mater. Sci.*, 2000, vol. 35, pp. 375–80.
21. C. Wang, Y. Wu, Y.A. Guo, J.T. Guo, and L.Z. Zhou: *J. Alloys Compd.*, 2019, vol. 784, pp. 266–75.
22. R. Marin, C. Hervé, J. Zollinger, M. Dehmas, B. Rouat, A. Lamontagne, N. Loukachenko, and L. Lhenry: *Metall. Mater. Trans. A*, 2020, vol. 51A, pp. 3526–34.
23. W.L. Wang, Z.J. An, S. Luo, and M.Y. Zhu: *J. Alloys Compd.*, 2022, vol. 909, p. 164750.
24. Y.B. Zhang, D.N. Zou, X.Q. Wang, Y.N. Li, Y.C. Jiang, and L.B. Tong: *J. Mater. Res. Technol.*, 2022, vol. 18, pp. 1855–64.
25. J. Zeng, C.Y. Zhu, W.L. Wang, and X. Li: *Metall. Mater. Trans. B*, 2020, vol. 51B, pp. 2522–31.
26. W.G. Jiang, J.S. Dong, and L. Wang: *J. Mater. Sci. Technol.*, 2011, vol. 27, pp. 831–40.

Publisher's Note Springer Nature remains neutral with regard to jurisdictional claims in published maps and institutional affiliations.

Springer Nature or its licensor (e.g. a society or other partner) holds exclusive rights to this article under a publishing agreement with the author(s) or other rightsholder(s); author self-archiving of the accepted manuscript version of this article is solely governed by the terms of such publishing agreement and applicable law.